Two-dimensional Lateral Epitaxy of 2H ($MoSe_2$) – 1T' ($ReSe_2$) Phases

Amey Apte,[1] Aravind Krishnamoorthy,[2] Jordan A. Hachtel,[3] Sandhya Susarla,[1] Jongwon Yoon,[4] Lucas M. Sassi,[1] Palash Bharadwaj,[5] James M. Tour,[4] Juan Carlos Idrobo,[3] Rajiv K. Kalia,[2] Aiichiro Nakano,[2] Priya Vashishta,[2] Chandra Sekhar Tiwary,[1†]* and Pulickel M. Ajayan[1]**

AUTHOR ADDRESS

1. Department of Materials Science & NanoEngineering, Rice University, 6100 Main Street, Houston TX – 77005, United States.
2. Collaboratory for Advanced Computing and Simulations, Department of Physics and Astronomy, Department of Computer Science, Department of Chemical Engineering and Materials Science, Department of Biological Sciences, University of Southern California, Los Angeles, CA – 90007, United States.
3. Center for Nanophase Materials Sciences, Oak Ridge National Laboratory, Oak Ridge, TN – 37831, United States.
4. Department of Chemistry, Rice University, 6100 Main Street, Houston TX – 77005, United States.
5. Department of Electrical and Computer Engineering,

Rice University, 6100 Main Street, Houston, TX – 77005, United States.

KEYWORDS

Two-dimensional materials, Heterostructures, transition metal dichalcogenides

ABSTRACT

Two-dimensional (2D) transition metal dichalcogenide (TMDC) heterostructures have been proposed as potential candidates for variety of applications like quantum computing, neuromorphic computing, solar cells, and flexible field effective transistors. The 2D TMDC heterostructures at the present stage face difficulties being implemented in these applications because of lack of large and sharp heterostructure interfaces. Herein, we address this problem via a CVD technique to grow thermodynamically stable heterostructure of 2H/1T' $MoSe_2$-$ReSe_2$ using conventional transition metal phase diagrams as a reference. We demonstrate how the thermodynamics of mixing in the $MoReSe_2$ system during CVD growth dictates the formation of atomically sharp interfaces between $MoSe_2$ and $ReSe_2$, which can be confirmed by high resolution scanning transmission electron microscopy imaging, revealing zig-zag selenium-terminated interface between the epitaxial 2H and 1T' lattices. Our work provides useful insights for understanding the stability of 2D heterostructures and interfaces between chemically, structurally, and electronically different phases.

TEXT

Two-dimensional materials such as graphene, boron nitride, transition metal dichalcogenides (TMDCs) / oxides (TMOs), etc. have exhibited interesting properties compared to their bulk counterparts. [1–9] Heterostructures of van der Waals' solids, which are composite materials made up of stacked atomically-thin two dimensional materials are also broadly studied. The idea, widely reviewed by Geim et al envisages a sequence of stacking individual two-dimensional materials on top of each other to realize certain increased chemical stability and emergent properties for applications. [10] A number of top-down and bottom-up techniques such as mechanical exfoliation, single/ multi-step vapor deposition, and wet chemical synthesis have been demonstrated for producing a variety of promising functional heterostructures such as graphene/TMDCs, TMDC/TMDC, metal/TMDC, etc. A few notable examples of such heterostructures includes MoS_2, WS_2, h-BN, or In_2Se_3 on graphene for novel photodetectors, MoS_2/WS_2 heterobilayers for two-dimensional field effect transistors and Pt or Ag/MoS_2 for electro-catalysis of hydrogen evolution reaction (HER) respectively. [11–17] Creating heterostructures by mechanical exfoliation results in extremely sharp and clean interfaces, but the coverage area is small and the method is only limited to non-epitaxial vertical stacking. [18] On the other hand, wet chemical synthesis results in large scale production of heterostructures with little control over quality. [19] Single and multi-step chemical vapor deposition (CVD) has been reported to give most reliable results; [20–23] As a result, a number of CVD techniques for growing MX_2 heterostructures (M = Mo/W, X = S/Se) have been reported and studied for their interesting band alignments, possibility of generating interlayer excitons and strong coupling, ultrafast charge transfer, and strain engineering. [23–29] However, the lateral and vertical heterostructure formation between the ubiquitous MoX_2/WX_2 system is considered to be a kinetic process, and

hence successful synthesis using CVD method depends on a lot of experimental variables such gas flow, position of precursors, time of evaporation of precursors etc. which makes it tricky to reproduce.

Adopting a thermodynamic approach for synthesizing heterostructures would be more beneficial as the process would be more controlled and easily reproducible and would result in a sharp interface. Using $ReSe_2/MoSe_2$ as a model system, we have designed a route to thermodynamically stable lateral TMDC heterostructures using the corresponding transition metal binary phase diagrams as a reference. Rhenium diselenide ($ReSe_2$) is a group VII transition metal dichalcogenide material which stabilizes in the distorted 1T (i.e. 1T') phase due to the presence of extra electron in the d-orbital of rhenium which hybridizes with the p-orbital of the chalcogen giving rise to octahedral coordination. [30,31] There is Peierls distortion in $ReSe_2$ which lowers the overall symmetry of this structure but causes the individual layers to be decoupled from each other even in bulk state, something that doesn't occur in Mo & W-based TMDCs. [31] Combination of $ReSe_2$ with $MoSe_2$ makes it a non-isomorphous system. Recently, we reported controlled doping of Re atoms in monolayer $MoSe_2$ lattice via chemical vapor deposition; steadily incorporating greater amount of Re destabilizes the 2H phase of $MoSe_2$ and instead results in the 1T' structure ($Re_{1-x}Mo_xSe_2$).[32] Such phase transformed alloys also exhibited emergent magnetism despite not being composed of conventional magnetic elements.

In this work, we report the synthesis and characterization of lateral heterostructure between monolayer $MoSe_2$ and $ReSe_2$ with 2H and 1T' symmetries respectively (referred to as 'RMS heterostructures'). The heterostructure was grown via chemical vapor deposition technique and characterized by a host of methods; the individual domains of single crystalline $MoSe_2$ are easily identifiable in a matrix of $ReSe_2$ via optical microscope and exhibit atomically sharp α-type

zigzag heterojunctions in high angle annular dark field scanning transmission electron microscopy (HAADF-STEM). Raman spectroscopy showed characteristic peaks for $MoSe_2$ & $ReSe_2$ lattices arising from their distinct symmetries. The Raman maps further clarified existence of a lateral heterostructure. X-ray photoelectron spectroscopy was used to identify the Re and Mo states and binding energies showing minimal doping. Density functional theory (DFT) simulations showed that the stable α interface representing the lowest energy configuration is non-magnetic and laterally delineates the monolayer 2H $MoSe_2$ and 1T' $ReSe_2$ domains with minimal cationic substitutions. Further, the formation of such a heterostructure results in dramatic reduction in band-gap with the valance & conduction band edge electronic states arising predominantly out of contribution from the molybdenum and rhenium atoms close to the atomically sharp interfaces. With the help of Mo-Re binary phase diagram, the reason for stability and large scale formation of this novel two-dimensional 2H-1T' heterostructure is explained.

The RMS heterostructures were grown via chemical vapor deposition (CVD) on single crystal sapphire (0001) substrates. The Mo and Re precursors were chosen as ammonium molybdate ($(NH_4)_2MoO_4$ Sigma Aldrich, 99.99%) and ammonium perrhenate (NH_4ReO_4, Sigma Aldrich, >99%) respectively. The relative ratio of the precursors was chosen as 2:1 by weight and they were placed in porcelain boats inside a 2" diameter quartz tube so as to reach temperatures of 600°C and 500°C respectively. Selenium powder (100 mesh, 99.99%) was chosen as the chalcogen source in a similar porcelain boat placed upstream in a temperature zone of ~250°C. The sapphire substrates were placed in a separate boat downstream of the precursor boats. The tube furnace was ramped up to 600°C in 20 min and held at that value for another 20 min before cooling down. High purity Ar/H_2 (15%) was used as the carrier gas for the growth. The

heterostructures were obtained on the top surface of the sapphire substrates and transferred onto SiO_2/Si substrates via standard "PMMA+KOH" etching for better visual identification.

Raman and PL spectra were obtained on an inVia spectrometer by Renishaw with 532 nm laser and 10 second acquisition times. XPS spectra were collected on a PHI Quantera system using 1486.6 eV incident X-ray energy and 26 eV pass energy. STEM experiments were performed on a Nion aberration-corrected UltraSTEM 100^{TM} operated at an accelerating voltage of 60 kV. The experiments were performed with a convergence semi-angle of 30 mrad. The HAADF image in Figure 2 (A) was a 2048x2048 pixel image with a 15 µs pixel dwell time over a 32 nm field-of-view (FOV). The HAADF image in Figure 2 (b and c) was 1024x1024 pixel image with a 15 µs pixel dwell time over a 16 nm FOV. In both images, a Gaussian blur with σ=1 is used to improve the signal-to-noise ratio.

DFT simulations of lateral interfaces were performed on systems containing 216 atoms, corresponding to 36 formula units each of $MoSe_2$ and $ReSe_2$, in a simulation cell measuring 40.2 Å $\times$ 19.7 Å along the *a*- and *b*-directions. DFT simulations of pure $MoSe_2$ and $ReSe_2$ and alloyed $Mo_{1-x}Re_xSe_2$ crystals for calculation of free energies were performed on supercells comprising $6 \times 6 \times 1$ unit cells containing 108 atoms. A vacuum of 15 Å is added along the *c*-axis of all simulation cells to remove spurious image interactions. Calculations were performed till each self-consistency cycle is converged in energy to within 1×10^{-5} eV/atom and forces on ions are under 1×10^{-2} eV/Å. Further details are given in Supplementary Information.

Figure 1 shows the schematic of the heterostructures and the synthesis setup. The molybdenum and rhenium precursors were kept in individual porcelain boats at different positions as described in the Methods section. The heterostructure samples were obtained on the

top surface of the sapphire substrate. However, to aid visual identification, the monolayers were transferred to a clean SiO_2/Si substrate (300 nm oxide layer) via standard PMM-mediated procedures reported in literature. Figure 1 (A) shows a 50X magnification optical image of the transferred sample. Two distinct spatial domains can be clearly identified – the darker (roughly) hexagonal islands are $MoSe_2$ whereas the lighter matrix surrounding them is $ReSe_2$. The $MoSe_2$ islands are approximately 10 microns large and have small multilayers at their centers. Figure 1 (B) shows the Raman spectra collected from the $ReSe_2$ (red) and $MoSe_2$ (blue) regions respectively; the $MoSe_2$ spectrum can be identified easily owing to the strong out-of-plane A_{1g} mode at ~ 239 cm^{-1}. The $ReSe_2$ spectrum is rich with at least 18 A_g Raman active vibrational modes (e.g. 124 cm^{-1}, 161 cm^{-1}, 176 cm^{-1}, etc.) due to the low symmetry of the $P\bar{1}$ space group and the distorted 1T phase. [33] This picture is made even clearer once we look at the Raman intensity maps in Figure 1 (C). The upper map at 239 cm^{-1} (green) shows only the hexagonal $MoSe_2$ crystal with a black background, whereas the lower map at 124 cm^{-1} (magenta) shows the $ReSe_2$ region. Photoluminescence spectra of $MoSe_2$ (shown in **Figure S1** in Supplementary Information) reveal a relatively weak and somewhat broad resonance at 1.56 eV which corresponds to the monolayer optical band-gap. This quenching of photoluminescence in the $MoSe_2$ region of the heterostructure is due to the donor-doping by Re atoms, which are thermodynamically predicted to be present in trace amounts in the $MoSe_2$ matrix and can be observed in atomic-resolution HAADF-STEM images (**Figure 2**). Previous studies have also demonstrated that small amounts of doping by donor atoms can lead to the formation of in-gap defect states leading to the reduction of the band-gap. [34] The atomic force microscopy (AFM) analysis in **Figures S2** & **S3** confirms the planar nature of the heterostructure, as shown in the Supplementary Information.

In order to understand the chemical composition of the heterostructure, the sample was studied with X-ray photoelectron spectroscopy. XPS is highly surface sensitive and can reveal information on the chemical bonding of the constituent atoms from the minor shifts in binding energies (B.E.) of their core electrons. Figure 1 (d-f) show the high-resolution XPS spectra of the Mo 3d, Re 4f, and Se 3d states respectively. The Mo 3d spectrum in Figure 1 (D) can be fit with two sets of $3d_{5/2}$ (lower B.E.) and $3d_{3/2}$ (higher B.E.) spin-orbit split peaks with a separation of 3.1 eV. The dominant $3d_{5/2}$ peak at 229.4 eV is due to Mo atoms predominantly in the 2H phase of $MoSe_2$ as reported. The other $3d_{5/2}$ peak occurring at a downshifted value of 228.6 eV could be due to Mo atoms in proximity to Re atoms either doped (lightly) in the $MoSe_2$ lattice or at the domain boundaries between the hexagonal islands and the surrounding matrix. Since Re atoms have extra electron, their presence next to Mo atoms causes increasing shielding of the nuclear charge of the latter which in turn decreases the binding energy of the Mo 3d electrons. The corresponding $3d_{3/2}$ peaks appear at 232.5 eV and 231.7 eV respectively. This is complemented by the Re 4f spectra in Figure 1 (E). The fitting yields a dominant $4f_{7/2}$ peak at 41.4 eV and weaker one at 41.9 eV respectively, which can be assigned to the 1T' phase of $ReSe_2$ (from the matrix) and for Re atoms at the heterojunction interfaces (and/or some light doping within the $MoSe_2$ lattices). The corresponding $4f_{5/2}$ pair of peaks appear with a separation of 2.45 eV at 43.8 eV and 44.3 eV respectively. Finally, we see that the Se 3d spectra in Figure 1 (F) shows an envelope that can be fitted with two pairs of peaks each with a mutual separation of 0.86 eV. These are attributed to the Se atoms bonding with Mo and Re atoms respectively.

To better understand the interface between the different phases of the heterostructures the monolayer samples are examined with a scanning transmission electron microscope (STEM).

Figure 2 (A) shows an atomic-resolution high-angle annular dark field (HAADF) image of a monolayer 1T'-$ReSe_2$ region surrounded by monolayer 2H-$MoSe_2$. We focus on an island of $ReSe_2$ surrounded by $MoSe_2$ to demonstrate the stability of the heterostructures, but larger uniform grains of both materials are observed throughout the sample. The center region shows the coordinated 4-anion unit-cell pattern of the 1T'-$ReSe_2$ phase, while outer regions show the hexagonal structure of the 2H phase. Additionally, the difference between the $ReSe_2$ and $MoSe_2$ can also be observed by the apparent brightness of the center region of Figure 2 (A), since HAADF images are formed through Z-contrast the heavy Re atoms (Z=75) are much brighter than the Mo (Z=42) and Se_2 (Z_{eff}=48.1) columns. Furthermore, it can be seen that the two phases are epitaxial to one another by taking the fast Fourier transform (FFT) of the image (shown in the inset). Here, the FFT spots all show the same hexagonal symmetry, if the $ReSe_2$ phase had any rotation with respect to the surrounding $MoSe_2$, a separate spot would be visible in the FFT. It can also be seen that the crystallographic orientation of the 2H phases on either side of the 1T' island are identical, further confirming the strong epitaxy of the heterostructure (**Figure S4**).

A higher resolution HAADF image of the interface between the 1T' and 2H regions is shown in Figure 2 (B). In the 2H-$MoSe_2$ region, there are many individual atoms that are much brighter than the other columns in the 2H lattice (a few have been highlighted with green arrows in Figure 2 (B)), indicating that Re atoms have diffused out into the 2H region. Likewise, it can be seen that on many of 4-anion unit cells near the surface in the 1T'-$ReSe_2$ only two or three of the anions are bright enough to be Re atoms (highlighted by orange arrows), indicating that Mo atoms have replaced them in the 1T' lattice. However, the interface between the two phases is atomically sharp, and moreover, extends as an atomically sharp region across large sections of the monolayer region. The area in the dashed box in Figure 2 (B) is shown in Figure 2 (C), and

the positions of all the atoms in the 2H phase and all the anions in the 1T' phase results are established and shown in Figure 2 (D).

The interface is unstable under the intense electron irradiation of the beam, as a result high-quality magnification images of the interface are difficult to achieve. This phenomenon is demonstrated directly in **Figure S5**, where the same interface can be seen to degrade from the zig-zag interface shown in Figure 2 (B-D), to an amorphous configuration in sequential images. This amorphization is also likely to be responsible for the high-contrast regions at the top of the image in Figure 2 (A).

Due to this instability, HAADF images are all acquired with short pixel dwell times and low pixel densities to minimize any perturbations to the crystal structure, and as a result many of the cation sites with smaller lattice spacings in the 2D projection cannot be resolved from one another. Rather than show some of the 1T' cation sites and not others, we have chosen to define the 1T' crystal just by the easily resolved anion sites. The fractional HAADF intensities of all the labeled sites are shown in Figure 2 (E), and show that red-sites are the Mo and the yellow sites are the Se_2 columns (due to the higher HAADF intensities), thus we can look back on the atom labeled image in Figure 2 (D) and see that the atomically sharp interface, takes place on the zig-zag plane and is Se terminated. Regardless of the instability under, the zig-zag termination is readily and consistently observed throughout the sample, moreover it is always observed to be atomically-sharp (Figure S6).

Figure 3 (A) shows the atomic arrangements in potential two interfacial structures along the low-energy zigzag direction, α and β, between monolayers of 1H $MoSe_2$ and 1T' $ReSe_2$. The α interface is characterized by the presence of 3-fold-coordinated Se anions at the $MoSe_2/ReSe_2$

interface, while the β interface contains only 4-fold coordinated Se ions at the interface following the terminology used by Lin et al for interfaces between 2H and 1T phases of MoS_2. [35] A comparison of the simulated interfacial structures with high-resolution TEM micrographs of the interface shows good correspondence between predicted and observed atomic positions for the α interface (Figure 3 (B)). This observation is also supported by DFT-computed interfacial energies for the α- and β-interfaces, which shows that the non-magnetic α interface represents the lowest energy configuration with an interfacial energy of 0.24 eV/Å, compared to 0.34 eV/Å (**Figure S7** in the Supplementary information).

To understand the composition of $MoSe_2$ and $ReSe_2$ crystals that constitute the experimental heterostructure and to quantify the extent of mutual doping, we calculate the free energy of alloyed $Mo_{1-x}Re_xSe_2$ monolayer crystals in the H and T' crystal structures from the DFT energies of formation and the analytical free energy of mixing (of Mo and Re ions) in the cation sub-lattice. The common tangent to these two free energy curves identifies the composition of H-phase $Mo_{1-\delta}Re_\delta Se_2$ and T'-phase $Re_{1-\delta}Mo_\delta Se_2$ ($\delta << 1$) crystals that are in chemical equilibrium across the interface in a lateral heterostructure. Figures. 3 (C) and (D) show that the lateral heterostructure is formed between a 2H $MoSe_2$ crystal containing 0.43% Re doping and a 1T' $ReSe_2$ crystal Mo substitutional defects in 1.73% of all cation sites, consistent with the experimentally observed marginal doping of Re atoms in $MoSe_2$ and vice versa (Figure 2).

The two-dimensional $Re_{1-x}Mo_xSe_2$ system can also be understood via metallurgical phase diagrams previously established in the literature. In order to understand the special nature of this system, we first consider the commonly studied 2D $W_{1-x}Mo_xX_2$ system (X = chalcogen). **Figure 4** (A) shows the binary Mo-W phase diagram. Molybdenum and tungsten are isomorphous and hence show complete miscibility at all compositions. Hence the phase diagram has (only) three

principal regions – solid solution, mixed solid solution + liquid, and complete liquid at higher temperatures. Therefore, the mixed alloy phase is thermodynamically preferred for this system at all compositions. Such transition metal atom substitution/ mixing in 2D TMDCs can be understood as every monolayer consists of three sublayers – a transition metal atom layer sandwiched between two chalcogen atom layers. Therefore, if the experiment consists of synthesizing 2D TMDC alloys, the mixing occurs only in the middle sublayer with the top and bottom chalcogen atom layers remaining intact. As a result, synthesizing 2D MoX_2-WX_2 heterostructures via CVD involves kinetic considerations such as changing the type and nature of the Mo & W precursors and growth temperatures to introduce substantial difference in evaporation times and rates so as to prefer the growth of one type of phase (MoX_2) before the other (WX_2). Another example is in the analysis of the 1D heterojunction between 2D $MoSe_2$ and WSe_2 heterostructures via atomically resolved HAADF-STEM imaging as reported by Huang et al. [28] They observe that the heterojunction shows a strong gradient of W atoms from the WSe_2 domain into the $MoSe_2$ one and vice versa. This phenomenon directly arises out of the isomorphous and miscible nature of molybdenum and tungsten.

On the other hand, the molybdenum-rhenium system is completely different. Figure 4 (B) shows the binary Mo-Re phase diagram. In stark contrast to the simplicity of the Mo-W system, the Mo-Re system shows rich phase mixing and segregation behavior as a function of temperature and composition. For instance, rhenium is (partly) miscible in molybdenum up to a maximum concentration Re ~ 40%. We have demonstrated this in our previous work on synthesizing 2D $Re_{1-x}Mo_xSe_2$ alloys with tunable composition via CVD. [32] At greater Re compositions, the binary system shows completely different structural phase(s) as shown in the figure. As we change fraction of Mo precursor over the Re one (in this work) while keeping the

rest of the growth parameters essentially unchanged, we find that the 2D $Re_{1-x}Mo_xSe_2$ system forms after which the molybdenum precipitates out of the solid solution to form distinct $MoSe_2$ domains inside of the $ReSe_2$-rich matrix, all at the monolayer level. This can be easily seen via Raman spectroscopy. Figure 4 (C) shows the optical images of five 2D $Re_{1-x}Mo_xSe_2$ samples; from left to right, the first three are alloys and the other two are segregated. Figure 4 (D) shows the corresponding Raman spectra of these five samples (from spots marked on the images in (C)). The strong A_{1g} mode from 2H $MoSe_2$ at ~240 cm^{-1} in Alloy A decreases in intensity with increasing Re concentration in Alloy B, and finally disappearing entirely for Alloy C with emergence of new modes. The fourth sample shows a heterostructure of triangular $MoSe_2$ domains dispersed in a matrix composed of Alloy C-type composition as shown from the distinct Raman spectra. This is an example of partial segregation and lies at the periphery of the blue and purple phases in the diagram in (B). For the fifth sample, the distinction is much stronger as the Raman spectra of the darker and lighter regions show complete phase segregation of $MoSe_2$ from $ReSe_2$. The dissimilarity between Mo and Re is also seen in the atomically resolved HAADF-STEM image in Figure 2 (C) with the sharp 1D junction between the $MoSe_2$ and $ReSe_2$ monolayers unlike the diffusion of Mo and W into each other as reported for monolayer $MoSe_2$-WSe_2 heterostructures.

The formation of a lateral heterostructure between semiconducting monolayer $MoSe_2$ and semimetallic monolayer $ReSe_2$ closes the band gap in the supercell containing the heterostructure interface. This reduction in band gap down from a value of 1.4 eV in monolayer $MoSe_2$ occurs via the formation of band-edge states at the valence and conduction edges. **Figure 5** (A) shows the partial density of electronic states in the $MoSe_2$/$ReSe_2$ heterostructure showing the contribution of interfacial Mo and Re atoms as well as 'bulk-like' atoms far away from the

interface. Figure 5 (A) shows that both valence and conduction band edge states arise from interfacial Mo and Re atoms, with bulk-like atoms contributing only negligibly to density of states in the range of (-0.6,0.1) eV around the Fermi level. Figures. 5 (B) and (C) depict the isosurface of the valence and conduction band-edge charge densities, showing spatial localization of these band-gap reducing states to within on lattice constant of the interface with little contribution from bulk-like atoms in the $MoSe_2$ or $ReSe_2$ monolayers.

In conclusion, we demonstrate the chemical vapor deposition synthesis of monolayer 2H $MoSe_2$ – 1T' $ReSe_2$ lateral heterostructures on single crystal sapphire substrates containing a smooth, atomically sharp interface along the zigzag directions between the parent phases as verified via high resolution HAADF-STEM imaging. Raman and XPS spectra show that the interface formed between the two nominally pure phases with negligible inter-diffusion of rhenium and molybdenum atoms. We also utilize the phase diagrams of the binary Mo-Re system to differentiate it from commonly reported Mo-W chalcogenide systems towards its unique thermodynamically-dictated preference for alloy vs heterostructure formation at the monolayer limit. This is supported by calculations of free energies and interfacial energies using Density Functional Theory, which also demonstrates how Mo and Re band edge states lead to strong reduction in electronic band gaps of the heterostructures. This work illustrates the use of atomic heterojunctions between two structurally and chemically distinct 2D materials as a potential method for tailoring the electronic structure for potential optoelectronic applications.

FIGURES

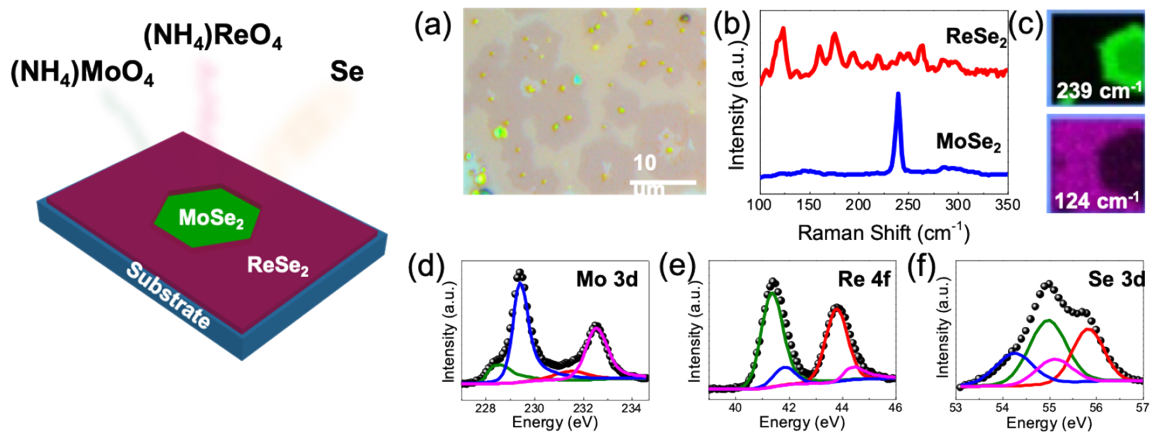

Figure 1. Synthesis and characterization of the $ReSe_2$-$MoSe_2$ heterostructures. (A) Optical image showing the monolayer $MoSe_2$ hexagonal flakes (dark) in monolayer $ReSe_2$ matrix(light). (B) Raman spectra of the two regions shows distinct signals corresponding to the $MoSe_2$ and $ReSe_2$ structures, which is confirmed by (C) spatial mapping; the green map shows the signal of 239 cm^{-1} mode of $MoSe_2$ (top) whereas the magenta map shows the 124 cm^{-1} mode of $ReSe_2$, confirming the heterojunction (D-F) High resolution XPS spectra showing presence of Mo 3d, Re 4f, and Se 3d signals in the synthesized samples.

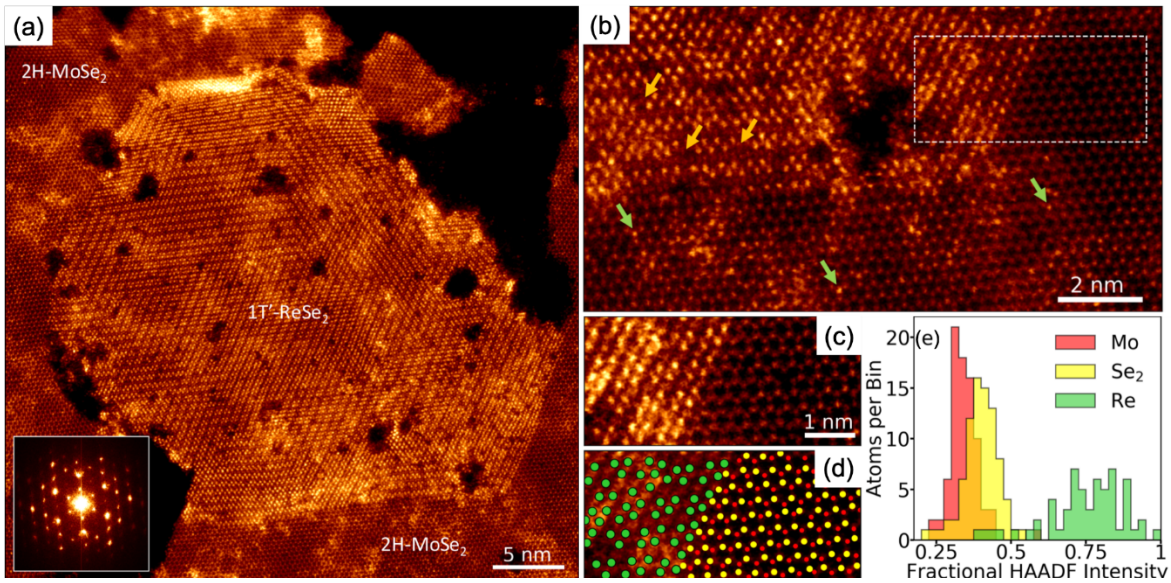

Figure 2. Atomic-resolution images of 1T'-$ReSe_2$ and 2H-$MoSe_2$ lateral heterostructures. (A) High-angle annular dark field (HAADF) scanning transmission electron microscopy (STEM) image of a monolayer heterostructures between 1T'-$ReSe_2$ and 2H-$MoSe_2$. Inset-fast Fourier transform of image in (A) showing epitaxial crystallinity between the two phases. (B) Higher resolution image of interface between $ReSe_2$ and $MoSe_2$. Some Mo atoms can be observed in 1T'-$ReSe_2$ lattice (orange arrows), and some Re atoms can be observed in 2H-$MoSe_2$ lattice (green arrows). Aside from a small degree of alloying the interface is atomically sharp. (C) Highlighted region from (B). (D) Atomic-site positions for all atoms in 2H phase and anions in 1T' phase. (E) Fractional HAADF intensities at the atomic positions in (D). It can be seen from relative HAADF intensities that red atoms are Mo, yellow atoms are Se, and green atoms are Re, indicating that the zig-zag type interface is Se terminated.

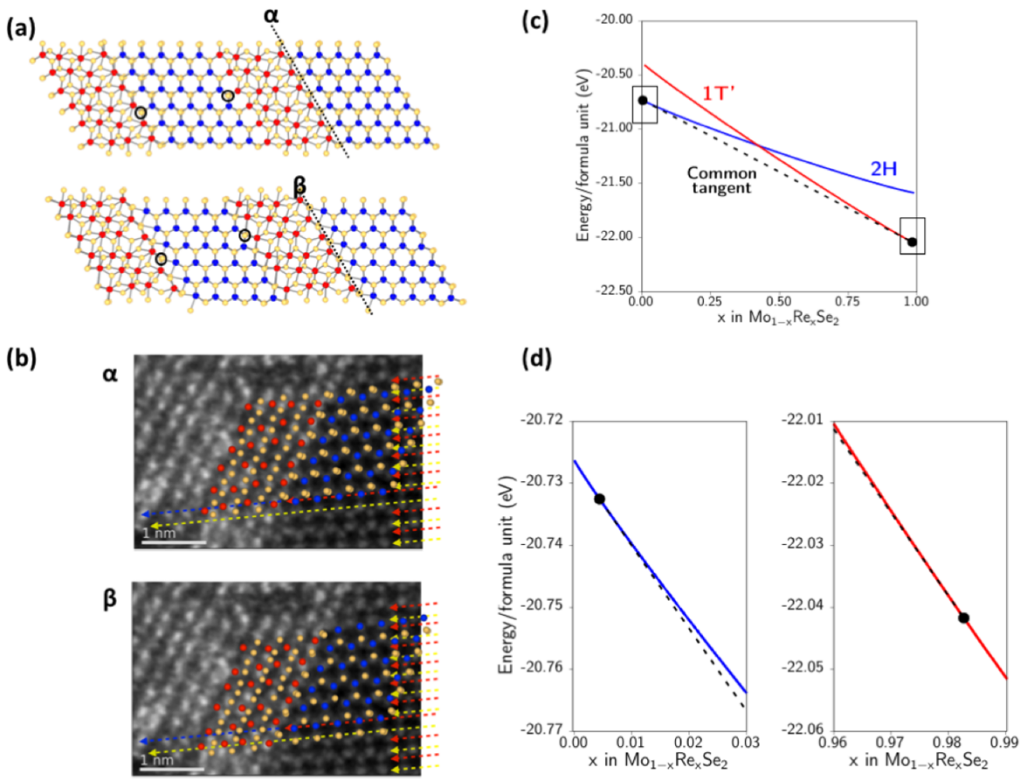

Figure 3. Structure and energetics of H-T' interfaces. (A) Atomic structure of the α (top) and β (bottom) interfaces between $MoSe_2$ and $ReSe_2$ monolayers. Representative 3-fold- and 4-fold-corordinated Se ions at the α and β interfaces are highlighted by circles. (B) High resolution scanning tunneling electron microscopy image of the $MoSe_2/ReSe_2$ interface overlaid with the computed atomic structure of the α and β interfaces shows better agreement between the observed experimental atomic positions and theoretical predictions in the α interfacial structure. (C) Common tangent construction between free energy curves of $Mo_{1-x}Re_xSe_2$ alloys in the H and T' crystal structures. Black dots denote the points of intersection of the common tangent between curves and (D) Zoomed-in views of highlighted areas near the common tangent intersections in (C) show that heterostructure formation occurs between 0.4% Re-doped $MoSe_2$ and 1.3% Mo-doped $ReSe_2$.

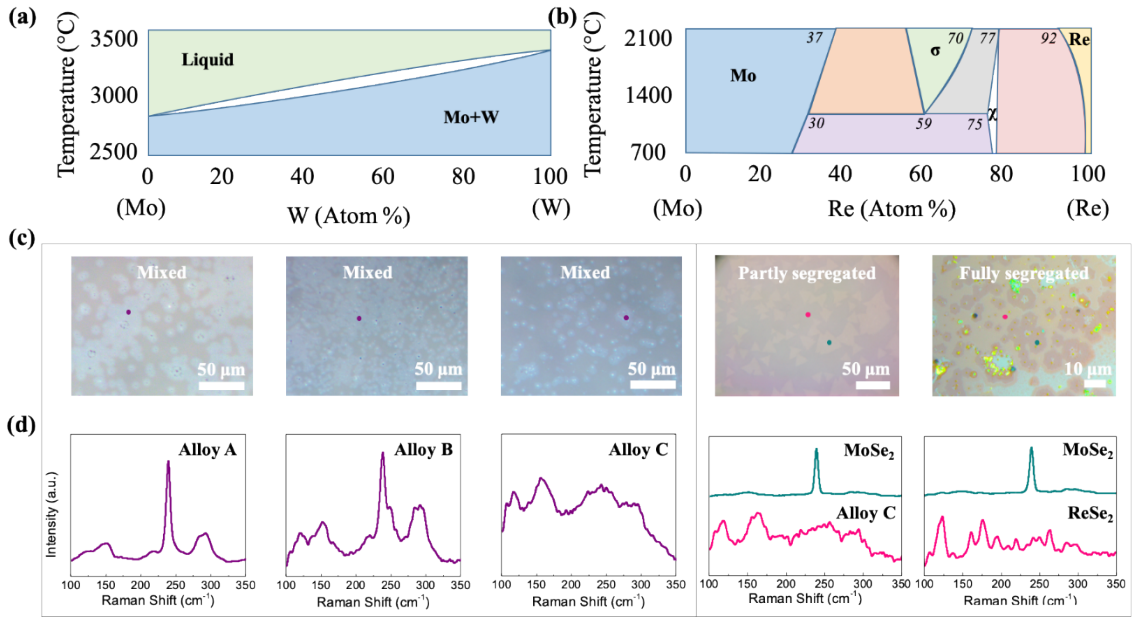

Figure 4. Mixing vs. segregation in the 2D molybdenum rhenium selenide system. (A) Binary Mo-W phase diagram (B) Binary Mo-Re phase diagram. The two diagrams illustrate the differences in miscibility of molybdenum with tungsten and rhenium respectively. (C) Optical microscope images of CVD-synthesized 2D $Re_{1-x}Mo_xSe_2$ samples with three alloy/mixed compositions (Re ~ 8%, 20%, and 40%) and two heterostructure/segregated compositions (Re > 40%) (D) Raman spectra of the five samples from the spots indicated in row (C) confirming gradual changes in composition and understood via phase diagram in (B). (Diagrams in (A) & (B) reproduced with permission from Springer Nature: "S.V. Nagender-Naidu et al. *Bulletin of alloy phase diagrams* Vol. 5, Issue 2, pp.177-180 ©1984" and "H. Okamoto, *Journal of Phase Equilibria (and Diffusion)* Vol. 31, Issue 6, pp. 580-581 © 2010", respectively).

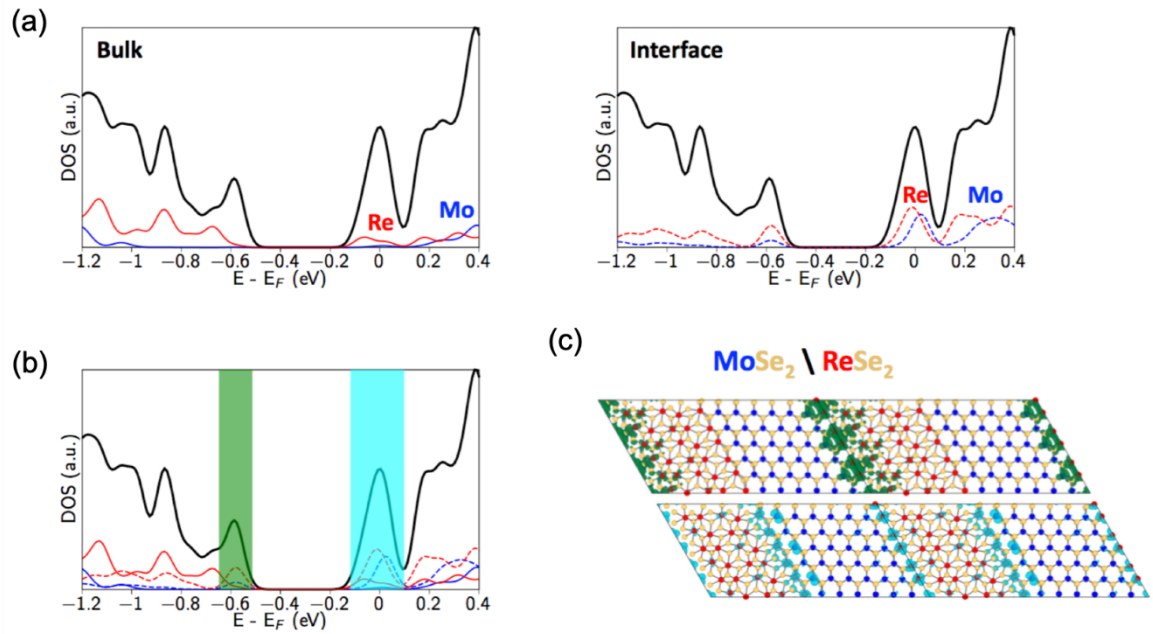

Figure 5. Electronic structure of lateral heterostructures. (A) Partial density of electronic states in the RMS heterostructure supercell, showing contributions from bulk-like (solid) and interfacial (dashed) atoms. It can be seen that interfacial Mo and Re atoms contribute significantly to the band edge states in both the valence and conduction bands, while the contribution from bulk-like atoms, particularly Mo, is negligible. (B, C) Isosurfaces of the spatial distribution of valence and conduction band edge states show that these band-gap reducing states are localized within one lattice constant from the $MoSe_2/ReSe_2$ interface.

ASSOCIATED CONTENT

Supporting Information.

The following files are available free of charge.

PL spectra, AFM images and analysis, additional HAADF-STEM images, device performance (PDF)

AUTHOR INFORMATION

Corresponding Author

priyav@usc.edu, cst311@gmail.com, ajayan@rice.edu

Present Addresses

†Metallurgical and Materials Engineering, Indian Institute of Technology, Kharagpur, West Bengal, India.

Author Contributions

AA synthesized the samples and performed the Raman/ PL measurements and device fabrication. SS performed XPS measurements. JAH and JCI performed STEM imaging and analysis. LS and PB helped with AFM measurements. JY and JMT performed electrical measurements. AK, AN, RKK, and PDV performed DFT simulations. PV, CST, and PMA advised the research. The manuscript was written through contributions of all authors. All authors have given approval to the final version of the manuscript.

Funding Sources

This work was supported by the Computational Materials Sciences Program funded by the U.S. Department of Energy, Office of Science, Basic Energy Sciences, under Award No. DE-SC0014607. Funding for the program of JMT has been provided by the Air Force Office of Scientific Research (FA9550-14-1-0111). Microscopy research conducted as part of a user proposal at the Center for Nanophase Materials Sciences, which is a DOE Office of Science User Facility.

Notes

REFERENCES

(1) Manzeli, S.; Ovchinnikov, D.; Pasquier, D.; Yazyev, O. V; Kis, A. *Nat. Rev. Mater.* **2017**, *2*, 17033.

(2) Wang, Q. H.; Kalantar-Zadeh, K.; Kis, A.; Coleman, J. N.; Strano, M. S. *Nat. Nanotechnol.* **2012**, *7*, 699–712.

(3) Ugeda, M. M.; Bradley, A. J.; Shi, S.-F.; da Jornada, F. H.; Zhang, Y.; Qiu, D. Y.; Ruan, W.; Mo, S.-K.; Hussain, Z.; Shen, Z.-X.; Wang, F.; Louie, S. G.; Crommie, M. F. *Nat. Mater.* **2014**, *13*, 1091.

(4) Geim, A. K.; Novoselov, K. S. *Nat Mater* **2007**, *6*, 183–191.

(5) Wang, X.; Gong, Y.; Shi, G.; Chow, W. L.; Keyshar, K.; Ye, G.; Vajtai, R.; Lou, J.; Liu, Z.; Ringe, E.; Tay, B. K.; Ajayan, P. M. *ACS Nano* **2014**, *8*, 5125–5131.

(6) Mann, J.; Ma, Q.; Odenthal, P. M.; Isarraraz, M.; Le, D.; Preciado, E.; Barroso, D.; Yamaguchi, K.; von Son Palacio, G.; Nguyen, A.; Tran, T.; Wurch, M.; Nguyen, A.; Klee, V.; Bobek, S.; Sun, D.; Heinz, T. F.; Rahman, T. S.; Kawakami, R.; Bartels, L. *Adv. Mater.* **2014**, *26*, 1399–1404.

(7) Alem, N.; Erni, R.; Kisielowski, C.; Rossell, M. D.; Gannett, W.; Zettl, A. *Phys. Rev. B* **2009**, *80*, 155425.

(8) Song, J.-G.; Ryu, G. H.; Lee, S. J.; Sim, S.; Lee, C. W.; Choi, T.; Jung, H.; Kim, Y.; Lee, Z.; Myoung, J.-M.; Dussarrat, C.; Lansalot-Matras, C.; Park, J.; Choi, H.; Kim, H. *Nat. Commun.* **2015**, *6*, 7817.

(9) Keyshar, K.; Gong, Y.; Ye, G.; Brunetto, G.; Zhou, W.; Cole, D. P.; Hackenberg, K.; He, Y.; Machado, L.; Kabbani, M.; Hart, A. H. C.; Li, B.; Galvao, D. S.; George, A.; Vajtai, R.; Tiwary, C. S.; Ajayan, P. M. *Adv. Mater.* **2015**, *27*, 4640–4648.

(10) Geim, A. K.; Grigorieva, I. V. *Nature* **2013**, *499*, 419–425.

(11) Lin, M.; Wu, D.; Zhou, Y.; Huang, W.; Jiang, W.; Zheng, W.; Zhao, S.; Jin, C.; Guo, Y.; Peng, H.; Liu, Z. *J. Am. Chem. Soc.* **2013**, *135*, 13274–13277.

(12) Gong, Y.; Lin, J.; Wang, X.; Shi, G.; Lei, S.; Lin, Z.; Zou, X.; Ye, G.; Vajtai, R.; Yakobson, B. I.; Terrones, H.; Terrones, M.; Tay, B. K.; Lou, J.; Pantelides, S. T.; Liu, Z.; Zhou, W.; Ajayan, P. M. *Nat Mater* **2014**, *13*, 1135–1142.

(13) Huang, X.; Zeng, Z.; Bao, S.; Wang, M.; Qi, X.; Fan, Z.; Zhang, H. *Nat. Commun.* **2013**, *4*, 1444.

(14) Chen, W.; Yang, Y.; Zhang, Z.; Kaxiras, E. *2D Mater.* **2017**, *4*, 45001.

(15) Lin, Y.-C.; Lu, N.; Perea-Lopez, N.; Li, J.; Lin, Z.; Peng, X.; Lee, C. H.; Sun, C.; Calderin, L.; Browning, P. N.; Bresnehan, M. S.; Kim, M. J.; Mayer, T. S.; Terrones, M.; Robinson, J. A. *ACS Nano* **2014**, *8*, 3715–3723.

(16) Yu, H.; Kutana, A.; Yakobson, B. I. *Nano Lett.* **2016**, *16*, 5032–5036.

(17) Lee, C.-H.; Lee, G.-H.; van der Zande, A. M.; Chen, W.; Li, Y.; Han, M.; Cui, X.; Arefe, G.; Nuckolls, C.; Heinz, T. F.; Guo, J.; Hone, J.; Kim, P. *Nat. Nanotechnol.* **2014**, *9*, 676.

(18) Liu, Y.; Weiss, N. O.; Duan, X.; Cheng, H.-C.; Huang, Y.; Duan, X. *Nat. Rev. Mater.* **2016**, *1*, 16042.

(19) Lei, Y.; Pakhira, S.; Fujisawa, K.; Wang, X.; Iyiola, O. O.; Perea López, N.; Laura Elías, A.; Pulickal Rajukumar, L.; Zhou, C.; Kabius, B.; Alem, N.; Endo, M.; Lv, R.; Mendoza-Cortes, J. L.; Terrones, M. *ACS Nano* **2017**, *11*, 5103–5112.

(20) Duan, X.; Wang, C.; Shaw, J. C.; Cheng, R.; Chen, Y.; Li, H.; Wu, X.; Tang, Y.; Zhang, Q.; Pan, A.; Jiang, J.; Yu, R.; Huang, Y.; Duan, X. *Nat Nanotechnol* **2014**, *9*, 1024–1030.

(21) Bogaert, K.; Liu, S.; Chesin, J.; Titow, D.; Gradečak, S.; Garaj, S. *Nano Lett.* **2016**, *16*, 5129–5134.

(22) Ullah, F.; Sim, Y.; Le, C. T.; Seong, M.-J.; Jang, J. I.; Rhim, S. H.; Tran Khac, B. C.; Chung, K.-H.; Park, K.; Lee, Y.; Kim, K.; Jeong, H. Y.; Kim, Y. S. *ACS Nano* **2017**, *11*, 8822–8829.

(23) Gong, Y.; Lei, S.; Ye, G.; Li, B.; He, Y.; Keyshar, K.; Zhang, X.; Wang, Q.; Lou, J.; Liu, Z.; Vajtai, R.; Zhou, W.; Ajayan, P. M. *Nano Lett.* **2015**, *15*, 6135–6141.

(24) Hong, X.; Kim, J.; Shi, S.-F.; Zhang, Y.; Jin, C.; Sun, Y.; Tongay, S.; Wu, J.; Zhang, Y.; Wang, F. *Nat. Nanotechnol.* **2014**, *9*, 682.

(25) Hill, H. M.; Rigosi, A. F.; Rim, K. T.; Flynn, G. W.; Heinz, T. F. *Nano Lett.* **2016**, *16*, 4831–4837.

(26) Chen, K.; Wan, X.; Wen, J.; Xie, W.; Kang, Z.; Zeng, X.; Chen, H.; Xu, J.-B. *ACS Nano* **2015**, *9*, 9868–9876.

(27) He, X.; Li, H.; Zhu, Z.; Dai, Z.; Yang, Y.; Yang, P.; Zhang, Q.; Li, P.; Schwingenschlogl, U.; Zhang, X. *Appl. Phys. Lett.* **2016**, *109*, 173105.

(28) Huang, C.; Wu, S.; Sanchez, A. M.; Peters, J. J. P.; Beanland, R.; Ross, J. S.; Rivera, P.; Yao, W.; Cobden, D. H.; Xu, X. *Nat. Mater.* **2014**, *13*, 1096–1101.

(29) Susarla, S.; Hachtel, J. A.; Yang, X.; Kutana, A.; Apte, A.; Jin, Z.; Vajtai, R.; Idrobo, J. C.; Lou, J.; Yakobson, B. I.; Tiwary, C. S.; Ajayan, P. M. *Adv. Mater.* **2018**, *0*, 1804218.

(30) Jariwala, B.; Voiry, D.; Jindal, A.; Chalke, B. A.; Bapat, R.; Thamizhavel, A.; Chhowalla, M.; Deshmukh, M.; Bhattacharya, A. *Chem. Mater.* **2016**, *28*, 3352–3359.

(31) Yang, S.; Tongay, S.; Li, Y.; Yue, Q.; Xia, J.-B.; Li, S.-S.; Li, J.; Wei, S.-H. *Nanoscale* **2014**, *6*, 7226–7231.

(32) Kochat, V.; Apte, A.; Hachtel, J. A.; Kumazoe, H.; Krishnamoorthy, A.; Susarla, S.; Idrobo, J. C.; Shimojo, F.; Vashishta, P.; Kalia, R.; Nakano, A.; Tiwary, C. S.; Ajayan, P. M. *Adv. Mater.* **2017**, *29*, 1703754.

(33) Wolverson, D.; Crampin, S.; Kazemi, A. S.; Ilie, A.; Bending, S. J. *ACS Nano* **2014**, *8*, 11154–11164.

(34) Ryder, C. R.; Wood, J. D.; Wells, S. A.; Hersam, M. C. *ACS Nano* **2016**, *10*, 3900–3917.

(35) Lin, Y. C.; Dumcencon, D. O.; Huang, Y. S.; Suenaga, K. *Nat. Nanotechnol.* **2014**, *9*, 391–396.